Element-to-tissue correlation in biological samples determined by three-dimensional X-ray imaging methods

Björn De Samber,[a] Geert Silversmit,[a] Karel De Schamphelaere,[b] Roel Evens,[b] Tom Schoonjans,[a] Bart Vekemans,[a] Colin Janssen,[b] Bert Masschaele,[c] Luc Van Hoorebeke,[c] Imre Szalóki,[d] Frank Vanhaecke,[a] Karen Rickers,[e] Gerald Falkenberg[e] and Laszlo Vincze*[a]

Synchrotron radiation based confocal micro-XRF was employed to unravel the tissue-specific three-dimensional (3D) distribution of metals down to trace concentration levels in a non-destructive manner within the crustacean *Daphnia magna*, an ecotoxicological model organism. Next to the analytical characterization of the employed confocal micro-XRF set-up, specific areas of metal accumulation in different cross-sections of interest within the organism were investigated. The use of a fast dynamic (continuous) scanning approach delivered 3D information on major, minor and trace element distributions in specific sub-regions within *Daphnia magna*. Coupling the obtained elemental information with microscopic morphological data obtained by laboratory absorption microtomography, full 3D element-to-tissue correlation could be derived, allowing a more detailed interpretation of the obtained results with respect to metal accumulation within this model organism.

Introduction

Synchrotron radiation X-ray fluorescence (SR-XRF) microbeam techniques at second- and third generation SR sources offer the potential of non-destructive multi-element analysis down to trace concentration levels with unrivalled spatial resolution among X-ray excitation based analytical techniques. At these sources, relative detection limits (DL) at the sub-ppm level can be achieved. With respect to absolute detection limits, sub-micron sized X-ray beams can offer DLs below 10 ag for the most efficiently excited transition elements, with a potential lateral resolution level better than 100 nm.[1,2]

These characteristics of microbeam SR-XRF allow spatially resolved multi-element determination of major, minor and trace constituents within biological specimens in an essentially non-destructive manner. In our previous work,[3,4] we illustrated the potential of this technique when investigating *Daphnia magna*, a frequently used ecotoxicological model organism. Fast dynamic micro-XRF (2D) scanning and XRF micro-CT experiments on these organisms allowed the semi-quantitative investigation of the accumulation of metals within specific organs with microscopic resolution. By combining SR-XRF and absorption micro-CT data sets on the same samples, it became possible to unravel the tissue-specific 2D/3D distribution of metals in situ

[a]Department of Analytical Chemistry, Ghent University, Krijgslaan 281, B-9000 Ghent, Belgium. E-mail: Laszlo.Vincze@UGent.be; Fax: +3292646699; Tel: +3292644822
[b]Laboratory of Environmental Toxicology and Aquatic Ecology, Ghent University, Jozef Plateaustraat 22, B-9000 Ghent, Belgium
[c]Centre for X-Ray Tomography, Department of Subatomic and Radiation Physics, Ghent University, Proeftuinstraat 86, B-9000 Ghent, Belgium
[d]Budapest University of Technology and Economics, Institute of Nuclear Techniques, Műegyetem rkp. 9, 1111 Budapest, Hungary
[e]Hamburger Synchrotronstrahlungslabor at DESY, Notkestr. 85, D-22603 Hamburg, Germany

within these delicate samples on the 3–15 μm resolution level in a non-destructive manner. With respect to toxicological effects, the determined tissue specific metal distributions (*e.g.* within ionoregulatory tissues and digestive tissues) is assumed to provide a further refinement and direct underpinning of so-called biotic ligand models (BLMs), which can be used to predict the metal toxicity as a function of metal concentration and physicochemical characteristics of the surface water.[5–9] On the basis of reliable BLMs, scientifically more relevant environmental regulations can be defined.

Due to the highly penetrating character of X-rays, conventional scanning micro-XRF yields integrated elemental distributions over the (element and matrix dependent) information depth within the sample, which are cumbersome to translate towards quantitative results when analysing a series of heterogeneous samples. Therefore it is more useful to analyse preselected cross-sections of toxicological relevance within the organism, *e.g.* dorsoventral sections containing the different organs/tissues of interest influenced by metal uptake. SR-XRF micro-CT allows the visualisation of (detectable) elemental distributions within selected virtual cross-sections through the sample, but the routine application of this technique on several samples is still too complex and the conversion of the obtained XRF data-sets towards quantitative results is challenging. The use of conventional 2D micro-XRF on thin tissue sections of known thickness represents a possible solution for simple and reliable quantification, but requires the use of complex sample preparation techniques which could influence the measured elemental distributions.

However, recently a new variant of the scanning micro X-ray fluorescence technique was developed, based on a confocal excitation/detection scheme using a polycapillary half-lens coupled with the energy dispersive detector which overcomes these problems. The detection volume defined by the intersection

of the exciting beam and the energy dependent acceptance of the polycapillary optics is ideal to perform non-destructive local analysis of the metal distributions inside delicate biological specimens, without the need of elaborate sample alignment, reconstruction methods or complex sample preparation.[10]

In what follows, the potential of this experimental technique is discussed within the framework of an ecotoxicological study on *D. magna* and a detailed characterisation of the employed confocal micro-XRF set-up is given. The ability of this technique to analyse the sample in different virtual planes and/or with a higher resolution is illustrated. Also, self-absorption effects inside the sample are visualised, which need to be corrected for during quantitative analysis. Next to this, the feasibility of a 3D dynamic scanning approach was investigated for confocal micro-XRF to image the trace level metal distributions in a tissue structure of interest.

Similarly to our previous works,[3,4] the confocal SR-XRF results are combined with laboratory X-ray absorption microtomography, which facilitates the interpretation of 3D elemental imaging results by providing a full 3D tissue-density model, *i.e.* an accurate frame of reference for the very same sample investigated by SR confocal micro-XRF. Complementary 3D absorption tomography allows the investigator to 'look inside' the sample, without the need of dissection, and to overlay distributions of the elements of interest on the tissue structure in order to investigate elemental associations and biological structure function relations.

Experimental

Sample preparation

D. magna were taken from the stock culture at the Laboratory of Environmental Toxicology of Ghent University. Details of the stock culture are described in ref. 11. The background Zn concentration in the culture water is about 5–7 µg Zn/L. An important requirement during a synchrotron micro-XRF experiment is the conservation of the sample upon irradiation. Next to mechanical rigidity, this also implies that there should be no translocation of elements on a scale comparable with the resolution used during the micro-XRF scan. Already in our previous work[3,4] we adapted a method by Tollrian *et al.*,[12] who used HMDS (1,1,1,3,3,3-hexamethyldisilazane) as a drying agent in a successful preparation method for scanning electron microscopy (SEM) investigations of daphnids.

Synchrotron radiation based confocal micro-XRF set-up

The scanning micro SR-XRF experiments were performed at Beamline L of the DORIS-III storage ring (4.45 GeV positron ring), HASYLAB (Hamburg, Germany). This beamline is dedicated to micro-XRF experiments, using either white or monochromatic bending magnet excitation and mono- or polycapillary focusing, and providing beam sizes of 5–20 µm FWHM.

In our experiments a Ni/C multilayer monochromator was used to obtain a 19.7 keV quasi monochromatic beam with a relative spectral bandwidth of $\Delta E/E = 1.83\%$. The primary beam was focused by means of a polycapillary optic having a working distance of 5 mm on the excitation side, providing a focused beam of 12 µm (FWHM). In order to obtain the element sensitive confocal volume, a novel strongly-focusing polycapillary half-lens was used on the detection side with a working distance of 2 mm, designed and manufactured by X-ray Optical Systems Inc.[13] This detector optic was aligned under a 90° angle relative to the incoming beam in the horizontal plane of the synchrotron storage ring. The detection side polycapillary was attached to a VORTEX-EX silicon drift detector (SDD) manufactured by SII NanoTechnology USA Inc. This detector had an active area of 50 mm[2] and a nominal crystal thickness of 350 µm. This energy-dispersive detector was coupled to a Canberra 2060 digital signal processor.

Next to sample visualisation and alignment using a long working distance optical microscope, the set-up also enabled micro-radiography using a high-resolution X-ray CCD camera (Photonic Science Coolview EM 1000, 1000 × 1000 pixels, 0.8 µm pixel size) under wide beam illumination, *i.e.* when the excitation side polycapillary was lowered and the detection side polycapillary retracted from the beam path.[14] The CCD camera proves to be very useful to localise histological regions of interest in X-ray transmission mode. This transmission X-ray camera could also be switched for an ionisation chamber in order to monitor the micro beam intensity behind the sample under focused beam conditions. An additional ionisation chamber in front of the polycapillary measured the intensity of the incoming beam, which was used for normalization purposes.

Fig. 1a shows a side view of the experimental set-up, with the synchrotron radiation emerging from the right. Behind the sample, the X-ray sensitive CCD camera mentioned above is installed which allows high resolution radiography (pixel size 0.8 µm). The sample stage comprises different motorised blocks for XYZ movement. Fig. 1b shows the top view of the experimental set-up: the monochromatized synchrotron radiation is focused by the excitation side polycapillary optic, positioned on a hexapod (PI) stage. The microbeam produced thus illuminates the sample, which is mounted on a goniometer head attached to the XYZ scanning/rotation stage. Fig. 1c provides a more detailed overview of the geometry of the samples (either *Daphnia magna*, NIST SRM 1577B biological standard or free standing thin film standard) with respect to the focusing and detection side polycapillaries, microscope and scanning motors. It should be noted that the size of the created confocal volume shown on Fig. 1c is enlarged with respect to the size of *Daphnia magna* for clarity purposes. In the figure, the FWHM acceptance of the detection side polycapillary optic is indicated by *a*, the FWHM of the microbeam generated by the polycapillary optic by *b* and the FWHM of a depth scan through the free standing thin film (FSTF) by *s*.

Laboratory based computed absorption microtomography

The scanning micro SR-XRF experiments were coupled with absorption microtomography measurements at the UGCT micro/nano-CT set-up at Ghent University, which was possible due to the excellent preservation of the samples during SR-XRF analysis. The UGCT facility offers the possibility to investigate a wide variety of samples with sizes ranging from a few micrometers up to several centimeters. A cone shaped X-ray beam is delivered by a FXE-160.50 dual head transmission X-ray
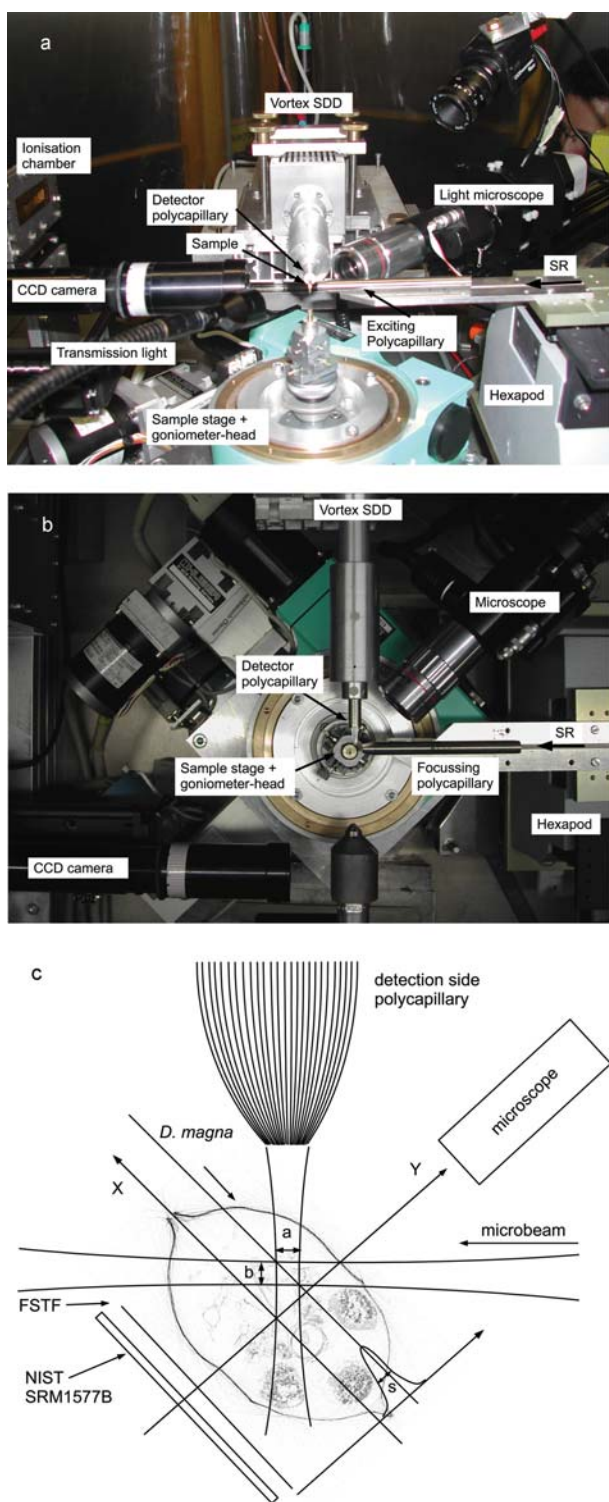
This journal is © The Royal Society of Chemistry 2010

J. Anal. At. Spectrom., 2010, **25**, 544–553 | 545

Fig. 1 A) Side view of the experimental set-up. B) Top view of the experimental set-up. C) Schematic representation of the confocal volume created by both polycapillaries.

was reconstructed using the Octopus software.[15] Three dimensional micro-CT images are then created using the VGStudio MAX software package.[29]

Results and discussion

Analytical characterisation of the synchrotron based confocal micro-XRF set-up

In order to convert the elemental intensity maps to reliable quantitative data, the confocal volume needs to be accurately determined.[16] A free standing thin film (FSTF) standard sample[17] was used in order to determine the acceptance of the detector side polycapillary optics. The applied thin-film standard can be considered as infinitely thin with respect to the beam size and confocal optic acceptance. The main advantage of the FSTF is that absorption effects can be neglected or have only a minor influence so that uncertainties in absorption or transmission do not influence the calibration in a significant way. As described in ref. 17, the FSTF standard exhibits a high level of uniformity with respect to elemental areal concentrations on both macroscopic and microscopic scales. A multi-element layer (Ca, Fe, Cu, Mo, La and Pb) was deposited on thin polymer foil by adequate physical vapour deposition (PVD) techniques such as magnetron sputtering, ion beam sputtering and pulsed laser deposition. The FSTF shows graded mass area densities in the (μg/cm^2) range. Accurate quantification was performed *via* microwave-assisted acid digestion using a mixture of HNO_3/H_2O_2. The elements were determined using a CirosCCD ICP-OES instrument from SPECTRO Analytical Instruments GmbH. These reference samples were characterized at the microfluorescence beamline L at HASYLAB. The homogeneity on a macroscopic scale (1 mm resolution) is better than 1%, whereas the micro homogeneity (5 μm resolution) is within statistical uncertainty of the measurement (2–4%). No sample degradation (*e.g.*, clustering for a given element) has been observed for a period of 5 months.

The element dependent acceptance was determined by scanning the FSTF through the confocal volume using a step size of 5 μm and a live time (LT) of 10 s/point. The sum spectrum corresponding to the scan through the multi-element FSTF standard can be seen in Fig. 2a. Spectral deconvolution of the individual XRF spectra has been performed by the nonlinear least-squares fitting software AXIL.[18] The batch processing of the individual XRF spectra was performed using the MicroXRF2 software package written in the IDL (Interactive Data Language) programming software.[30] The determined confocal scan profiles for the elements present in the FSTF standard are shown in Fig. 2b. After performing a non-linear least-squares fit of these element dependent scan profiles to a Gaussian function, the FWHM of the line scan s is obtained. The energy dependent acceptance a of the detection side capillary is then determined by the following formula, taking into account the convolution of the excitation side and detection side capillary beam profile when the FSTF standard moves through the confocal volume:

$$a = \sqrt{2s^2 - b^2} \qquad (1)$$

where b represents the FWHM of the beam size of the excitation side capillary as shown in Fig. 1c. The energy dependent

tube (160 kV, 900 nm focal spot size) from Feinfocus. Several hundreds of magnified radiographs of the sample are recorded by a Rad-Eye HR CMOS detector, equipped with a Gadox scintillation screen (1200 × 1600 pixels). The projection data-set (typically 800 projections, 40 flat field images and 5 offset images)
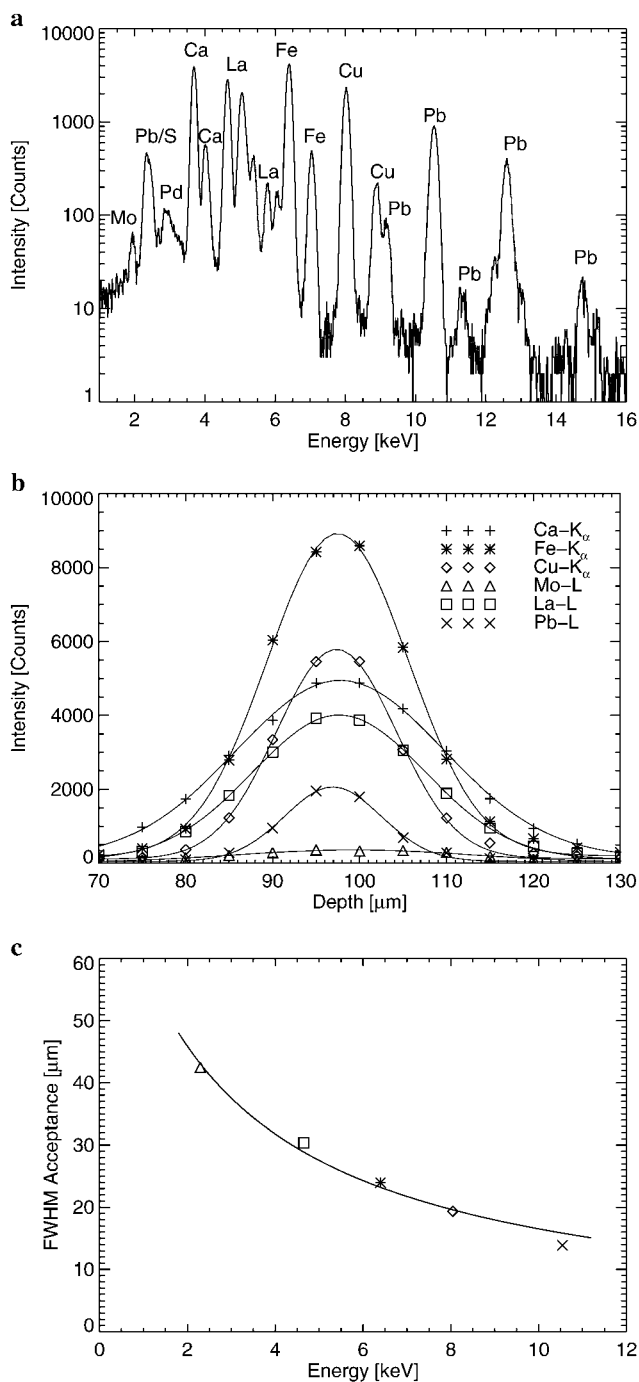
Fig. 2 A) Sum spectrum of the line scan measurement of the FSTF multi element standard (LT = 360 s). B) Elemental intensities of Ca, Fe, Cu, Mo, La and Pb during a depth scan through the free standing thin film (FSTF) multi element standard (36 × 5 μm step size, LT = 10 s/point). C) Acceptance determination of the detector polycapillary using a depth scan through the FSTF standard.

acceptance of the detection side polycapillary is shown in Fig. 2c by plotting the determined acceptance of the detection side capillary as a function of the characteristic fluorescent line energy.

Although these FSTFs are also suited for the calibration of the elemental sensitivities, we preferred the use of NIST SRM 1577B (Bovine Liver) pressed pellets in order to obtain a representative

elemental yield curve. The elements present in this SRM and its matrix composition are more representative to the organic samples which were the subjects of this study.

In order to minimize self-absorption effects within the NIST SRM 1577B material, confocal XRF spectra at a position were measured where absorption effects were minimal. This position was established by a depth scan through the sample, as illustrated in Fig. 3a. By approximation, the center of the confocal volume is coinciding with the surface of the sample at the position where the total incoming count rate is half of the maximum value obtained in the total depth scan. Since the relative distance between the maximum count rate and half of its intensity is approximately 20 μm, we can say that the energy dependant confocal volume for the main constituent of the SRM (potassium) was positioned just below the surface of the SRM. It should be noted that a depth scan through the SRM not only reveals the position of the sample surface and its total thickness (~150 μm) but, at the same time, the obtained depth profiles give a good indication of the self-absorption effects within this SRM. Fig. 3b shows the typical confocal XRF spectrum of the NIST SRM1577B (LT = 1000 s, normalised to a DORIS-III current of 100 mA), measured at the position with maximum incoming count rate, *i.e.* where the confocal volume is just below the sample. At higher energies, one can observe a lower count rate as compared to a conventional detection mode, which is due to the high energy filtering effect of the detection side polycapillary.

The calculation of the minimum detection limit (MDL) is based on the standard counting deviation based on Poisson statistics ($\sigma = \sqrt{I}$, where I is the detected counts in a given measuring time) and is defined as the amount of analyte that gives a net intensity equal to three times the standard counting error of the background intensity. Assuming a mass concentration c_i for element i for the given SRM (*e.g.* in ppm), the minimum detection limit (in terms of mass concentration c_i) for element i can be expressed as:

$$MDL_i = \frac{3\sqrt{I_B}}{I_i} \times c_i \qquad (2)$$

where I_i represents the net fluorescent line intensity and I_B the background intensity of the considered element i. The MDL can also be expressed in terms of absolute elemental mass m_i, although this requires the estimation of the mass probed by the confocal volume, which can be approximated using the following formula:

$$m_i = c_i \times \rho \times V_C \qquad (3)$$

where ρ is the sample density (in μg/cm³) and V_C represents the estimation of the confocal volume (in μm³). Using the previously determined energy dependent acceptance FWHM (a) of the detection side polycapillary and the FWHM ($b \approx 12\mu m$) of the beam size generated by the excitation side polycapillary, the confocal volume V_C can be approximated by:

$$V_C = \frac{\pi}{4}ab^2 \qquad (4)$$

The density ρ of the NIST SRM 1577B pressed pellet reference material used for the MDL determination can be approximated by dividing the total mass of the pellet by its total volume, which
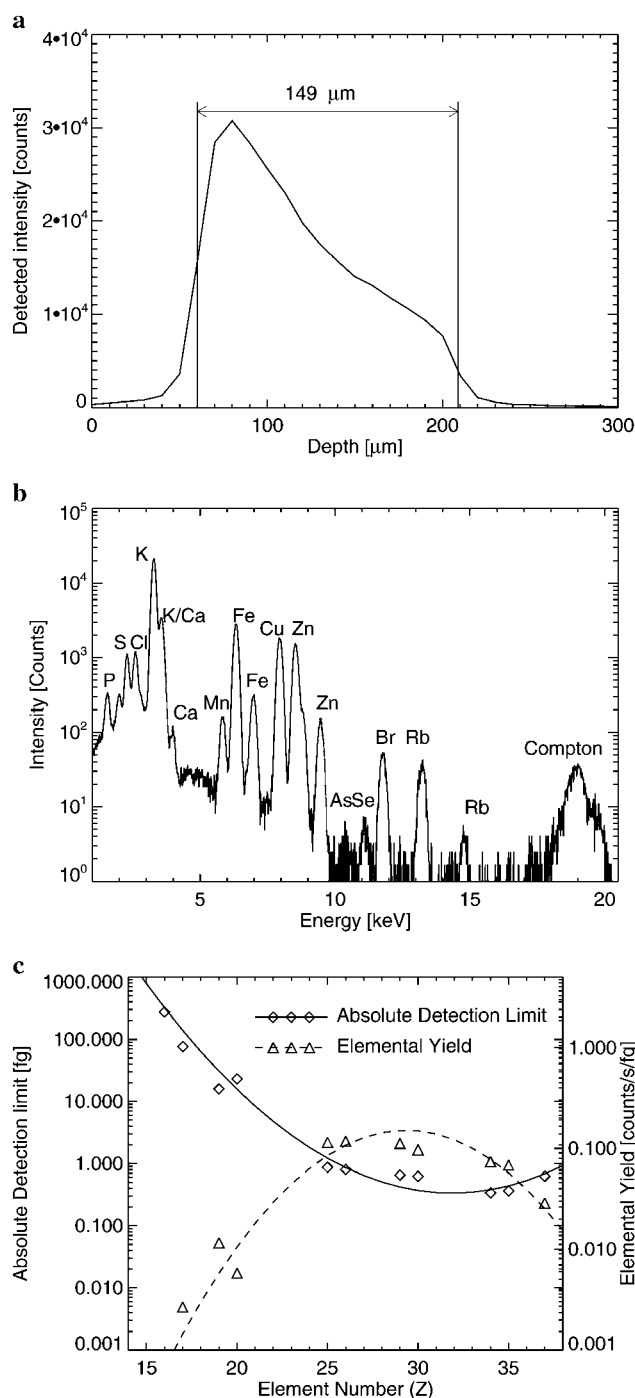
This journal is © The Royal Society of Chemistry 2010

J. Anal. At. Spectrom., 2010, **25**, 544–553 | 547

intensity for a specific element per second originating from the confocal volume:

$$Y_i = \frac{I_i}{T_{live}} c_i^{-1} \qquad (5)$$

where T_{live} is the measuring live time which results in a detected (net) line intensity I_i for element i. Similarly to the calculation of the MDLs, the elemental yield can also be expressed in terms of absolute elemental mass m_i (*e.g.* in counts/(s/fg)).

Fig. 3c shows the elemental yield and absolute detection limits determined using the NIST SRM 1577B sample for a live time of 1000 s, taking into account the energy dependence of the detector polycapillary acceptance as illustrated in Fig. 2c. For the most sensitive elements, absolute detection limits are in the 0.5 fg range, corresponding to relative detection limits of approximately 100 ppb.

Self-absorption effects within *Daphnia magna*

Due to the confocal principle, local fluorescence is collected from a well-defined volume within the sample. For a specific element, both K_α and K_β lines are collected. The ratio of these K_α and K_β lines can be calculated for each atomic number by using their corresponding radiation rates, *e.g.* by using the XrayLib database.[19] Since the attenuation coefficient for a K_α line is higher than for K_β,[31] their corresponding intensity K_α/K_β will be reduced if significant absorption is occurring, which is the case when the confocal volume is extracting information from deeper regions within the sample. Therefore, the intensity of the K_α and K_β lines gives an estimate of the importance of absorption effects in the sample as the analysing confocal volume moves deeper into the sample.

In order to verify possible self-absorption effects on the previously discussed dorsoventral sections on *Daphnia magna* which could interfere with the interpretation of the results, the Ca-K_α and Ca-K_β peaks were fitted separately for all individual measuring points using the AXIL and MicroXRF2 software packages.[18] In Fig. 4, the Ca-K_α/Ca-K_β ratio is visualised using the IDL software package.[30] The orientation of the excitation and detection side polycapillary is also indicated. A clear
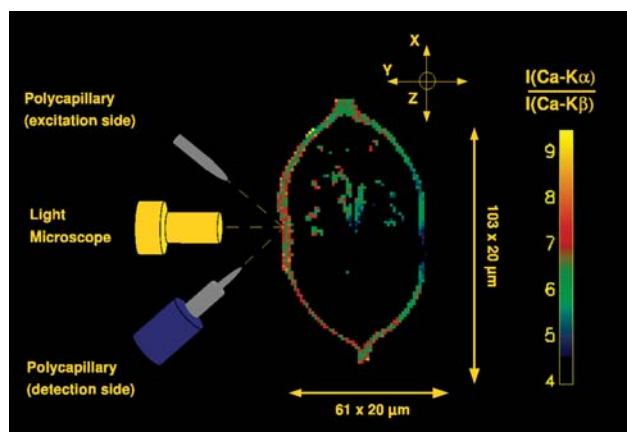
Fig. 3 A) Depth scan through an NIST SRM 1577B pressed pellet of *ca.* 150 μm thickness. B) Sum spectrum measured at the surface of NIST SRM 1577B (LT = 1000 s). C) Elemental yields and absolute detection limits of the experimental set-up derived from the NIST SRM 1577B pellet.

is known since the thickness can be determined by a confocal depth scan shown in Fig. 3c and the diameter of the pressed pellet is defined by the properties of the press (in our case 13 mm diameter).

Besides the MDLs, also the elemental yield Y_i for element i (in terms of mass concentration c_i) can be calculated, which provides valuable information on the detected fluorescent line

Fig. 4 Variation of the $Ca_{K\alpha}/Ca_{K\beta}$ intensity ratio in *Daphnia magna*. The orientation of both polycapillary optics and motors with respect to the sample is indicated.

gradient in the Ca-K$_\alpha$/Ca-K$_\beta$ ratio can be observed: it drops from 8.8 at the side of the carapace closest to the detection side polycapillary to 4.7 at the side of the carapace furthest from the detection side polycapillary, which is in perfect agreement with what one would expect on the basis of self-absorption effects. Also note, that the maximum value for the Ca-K$_\alpha$/Ca-K$_\beta$ ratio is in good agreement with the theoretical value when no self-absorption effects are occurring.

The Ca-K$_\alpha$/Ca-K$_\beta$ ratio can also be used to predict the magnitude of absorption effects for the other elements. If we consider R to be the measured (self-absorption modified) line ratio $I_{K\alpha}/I_{K\beta}$ for a given element, we can apply the X-ray attenuation law as follows:

$$R = \frac{I_{K_\alpha}}{I_{K_\beta}}$$
$$= R_0 e^{-(\mu_{K_\alpha} - \mu_{K_\beta})d} \qquad (6)$$
$$= R_0 e^{-\Delta\mu_{K_\alpha - K_\beta}d}$$

where R_0 is the line ratio without self-absorption effects, d the effective sample depth from which the signal originates. The difference in mass attenuation coefficients $\Delta\mu_{K\alpha-K\beta}$ can then be estimated by approximating μ as being proportional with $1/E^3$, that is:

$$\Delta\mu_{K_\alpha - K_\beta} = \mu_{K_\alpha} - \mu_{K_\beta}$$
$$= \mu_{K_\alpha} - \mu_{K_\alpha}\left(\frac{E_{K_\alpha}}{E_{K_\beta}}\right)^3$$
$$= \mu_{K_\alpha}\left(1 - \frac{E_{K_\alpha}^3}{E_{K_\beta}^3}\right) \qquad (7)$$
$$= \mu_{K_\alpha}\left(1 - k^3\right)$$

where $\mu_{K\alpha}$ and $\mu_{K\beta}$ are the mass attenuation coefficients at the fluorescent line energies $E_{K\alpha}$ and $E_{K\beta}$, respectively. By combining eqn (6) and eqn (7), the exponent in the attenuation term for the K$_\alpha$ fluorescent line can be estimated as follows:

$$\ln\left(\frac{R}{R_0}\right) = -\mu_{K_\alpha}d\left(1 - k^3\right)$$
$$\mu_{K_\alpha}d = \frac{\ln\left(\frac{R_0}{R}\right)}{1 - k^3} \qquad (8)$$

From eqn (8), the effective transmission for the various fluorescent lines can be calculated, showing that in case of Ca-K$_\alpha$ fluorescence approximately 17% of the fluorescent signal emerges from the sample, whereas the effective transmission for Zn-K$_\alpha$ fluorescence is 87%. From this we can conclude that the obtained semi-quantitative results for the Zn-concentrations are not influenced significantly by absorption effects.

High resolution 2D confocal micro-XRF combined with 3D absorption micro-CT data-sets

Fig. 5 illustrates the powerful capability of confocal micro-XRF to investigate smaller, local areas of metal accumulation within the sample, characterized by larger overview confocal XRF scans. First, a dorsoventral section through *Daphnia magna* was
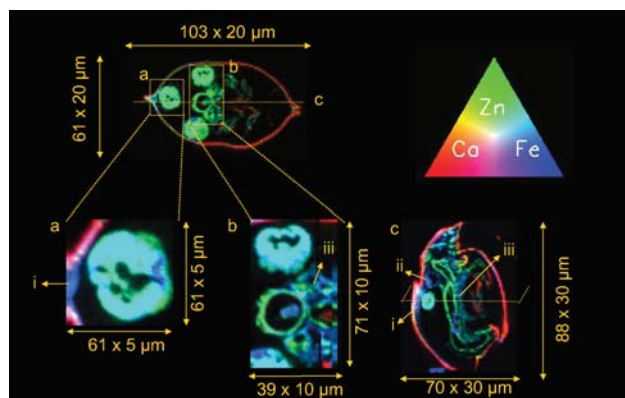

Fig. 5 Illustration of the local analysis capabilities of confocal micro-XRF. The top image shows a dorsoventral scan through *Daphnia magna* (step size 20 μm). Detail 1 shows a scan of the egg (step size 5 μm). Detail 2 shows a detail of the gut and gill tissue (step size 10 μm). Detail 3 shows a sagittal scan through the sample. ((i) Dorsal ridge of carapace; (ii) pericardium; (iii) ovary.)

analysed to obtain a general overview of the elemental distributions. In order to provide maximum information within a single image, the colours red, green and blue were scaled to the Ca, Zn and Fe intensities (which are proportional to the elemental concentrations) using the IDL software package.[30] After the overview scan, different sub-regions of interest, such as eggs (Fig. 5.a), gut and gill tissue (Fig. 5.b) were analysed in more detail by using smaller scanning steps (*e.g.* respectively 5 or 10 μm instead of 20 μm) or longer measuring times per voxel (*e.g.* 3 s/voxel instead of 2 s/voxel). Although the energy dependent acceptance of the detection side polycapillary is larger than the minimal step size used (5 μm), it is useful to choose the step-sizes as half of the beam size and half of the minimal detection side polycapillary acceptance, *i.e.* approximately 5 μm in our case.

An important aspect of confocal micro-XRF is that the elemental distributions in different planes of interest can be analysed easily. In Fig. 5.c, a sagittal section through the very same sample is visualised, enabling it to link specific metal accumulation patterns to corresponding biological/physiological features. Note, for example, that the Fe distribution in this figure matches the main sites of haemoglobin concentration in the circulatory system of the organism. Haemoglobin is a porphyrin-Fe complex which can capture oxygen from the surrounding medium and acts as an oxygen-transport molecule throughout the organism's tissues. Different haemoglobin currents inside the organism become confluent at the median dorsal ridge of the carapace (see Fig. 5.a.i & Fig. 5.c.i) before returning to the pericardium around the heart (see Fig. 5.c.ii).[20,21] The Fe detected at the base of the sample is due to the trace level presence of Fe in the glass support capillary. Regarding the reproductive toxicity of dietary Zn exposure[5] (see next section), it would also be interesting to gain a more detailed analysis of the ovary located in the front of the gut (see Fig. 5.b.iii & Fig. 5.c.iii).

After the synchrotron based confocal-XRF measurements, the sample was also analysed using laboratory micro-CT, providing 3D density (absorption coefficient) data of *Daphnia magna*. The dorsoventral and sagittal elemental distributions of *Daphnia magna* shown in Fig. 5 were combined and rendered together with the laboratory micro-CT dataset using the VGStudio MAX
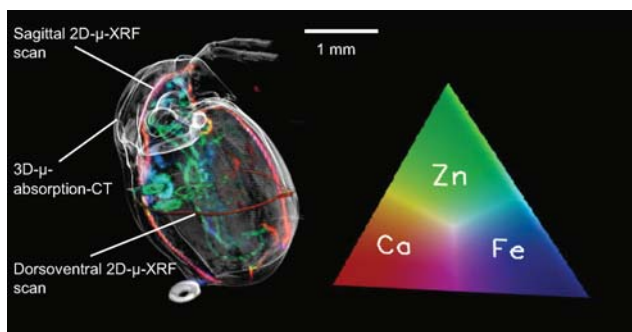
This journal is © The Royal Society of Chemistry 2010

J. Anal. At. Spectrom., 2010, **25**, 544–553 | 549

Fig. 6 Combination of laboratory absorption micro-CT and SR 2D confocal micro-XRF data sets on *Daphnia magna* (dorsoventral and sagittal plane).

software package.[29] This allows the combination of the 2D elemental information (obtained by SR confocal micro-XRF) with the 3D internal structure/morphology of the sample (obtained by laboratory micro-CT), as illustrated in Fig. 6. Further in this article, a full 3D comparison between elemental and absorption datasets on the micrometer scale will be illustrated by means of a dedicated 3D confocal scanning routine.

Investigation of Zn accumulation in *D. magna* by continuous scanning confocal micro-XRF following exposure to elevated Zn levels

An ecotoxicological experiment was performed to determine in which tissues Zn accumulation occurs following exposure of *D. magna* to an elevated Zn concentration. *Daphnia magna* were cultured for 16 days as explained in Muyssen *et al.*[11] in a medium containing a background of 5 µg Zn/L (unexposed *Daphnia*) and also in a medium with elevated Zn (340 µg/L) (exposed *Daphnia*). Dynamic scanning confocal µ-XRF was used to obtain virtual dorsoventral sections of both samples. The results of the analysis

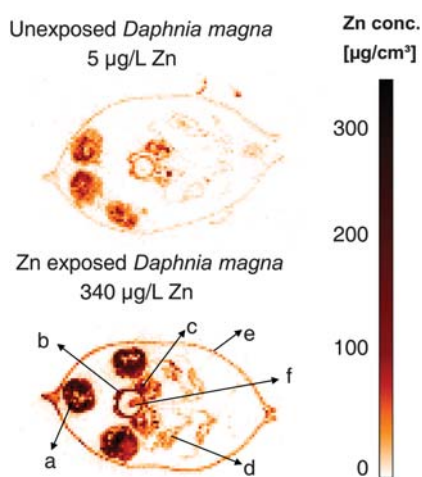**Fig. 7** Dorsoventral sections through *Daphnia magna* obtained by SR 2D confocal micro-XRF. The samples originated from a medium containing 5 µg Zn/L (unexposed *Daphnia magna*) and 340 µg Zn/L (exposed *Daphnia magna*). A color bar shows the volume concentration in µg/cm³. The different tissues are indicated: (a) egg; (b) gut epithelium; (c) ovary; (d) thoracic limb with gill tissue; (e) carapace; (f) gut lumen.

are shown in Fig. 7. A color bar on the right gives an estimation of the volume concentration in µg/cm³ by dividing the intensity map by the elemental yield Y observed for the NIST SRM 1577B (based on the volume concentration). These values could in principle be converted to a mass concentration (*e.g.* µg/g) if additional information concerning the density of the sample is obtained.

Comparison of exposed and non-exposed *Daphnia* shows a distinct accumulation in several tissues: *i.e.* the eggs (Fig. 7.a), gut epithelium (Fig. 7.b), ovaries (Fig. 7c), gills (Fig. 7.d) and the carapace (Fig. 7.e) of the exposed *Daphnia*. Physiological research suggests that Zn uptake in fish from the water mainly occurs *via* the gill tissue, where it interferes with Ca homeostasis which ultimately leads to toxicity.[22–24] It is possible that this is also the case in *Daphnia* and that Zn first enters the gill tissue, interferes with Ca homeostasis (as suggested by Muyssen *et al.*[11]) and is then further distributed into other tissues of possible toxicological relevance. It is also possible that Zn enters tissues after being taken up *via* the diet. Indeed, *Daphnia* feed on live green algae during the exposure. Since algae can accumulate Zn they provide a potential source of Zn accumulation *via* ingestion by *Daphnia*. Further research will aim at specifically discriminating between both exposure routes (water *vs.* diet). Finally, the accumulation in both ovaries and eggs suggests that the distinct accumulation in the eggs is at least explained by accumulation during their residence in the ovary. However, it cannot be excluded that part of the Zn observed in the eggs has been accumulated during their stay in the brood chamber, where they are exposed to the culture water through brood pouch ventilation.[25] These first results illustrate that this technique will become a valuable tool in establishing a link between accumulation of metals in specific tissues and toxicological responses.

Combination of 3D confocal micro-XRF and absorption micro-CT on *Daphnia magna*

Full 3D determination of elemental distributions based on micro-XRF computed tomography (micro-XRF CT) has been demonstrated by several groups.[26,27] In general, micro-XRF CT involves long measuring times and challenging data treatment, making a 3D determination/visualisation of the elemental distributions within a given sample a complex task. In contrast, confocal micro-XRF does not require a tomographic reconstruction procedure, and it enables the local analysis of arbitrary sub-volumes inside the sample. Illustrations of fully 3D confocal micro-XRF imaging have been reported in the past,[28] although the applied non-continuous scanning algorithm limits the size of the sample which can be visualised. Therefore, with the adaptation of the scanning strategy for fast 2D dynamic scanning, involving the possibility to scan different sample planes by continuous movements, a practical way of 3D confocal micro-XRF becomes feasible. In order to illustrate this dynamic scanning approach, a single egg was extracted from a *Daphnia magna* sample and attached to a carbon fibre. The sample was pre-characterised using absorption micro-CT, using the same laboratory set-up as previously described. Fig. 8 clearly illustrates the rough surface of the sample and surface interface between the glue and the supporting fibre. Fig. 9 shows the elemental distributions of Zn (Fig. 9.a), Fe (Fig. 9.b), Ca (Fig. 9.c) and Compton
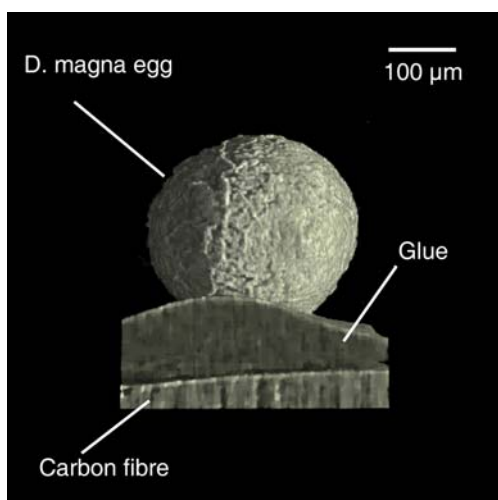
Fig. 8 Laboratory absorption micro-CT scan on an extracted egg of *Daphnia magna* attached with glue to the carbon support fibre. The diameter of the sample is about 300 μm.

scattering (Fig. 9.d) of a single plane through the egg. The step size of the vertical and horizontal motors was 5 μm, resulting in a total amount of 3953 single spectra (LT = 1 s). As the beam size and the acceptance of the detection side capillary for the higher Z elements are both in the 10 μm range, as illustrated by Fig. 2c, taking step sizes to be half of these dimensions (*i.e.* 5 μm) is considered to be a good compromise.

It can be observed that the Zn (Fig. 9.a) and Fe (Fig. 9.b) distributions are very similar. It can be noted that Fe seems to be somewhat more heterogeneously distributed in comparison with Zn in the centre of the egg, featuring some hot spots at the base of the sample. Similar areas can be observed where a very low count rate is detected, probably indicating hollow areas inside the sample (Fig. 9.a–d.i–iii). Also the Ca distribution shows the same
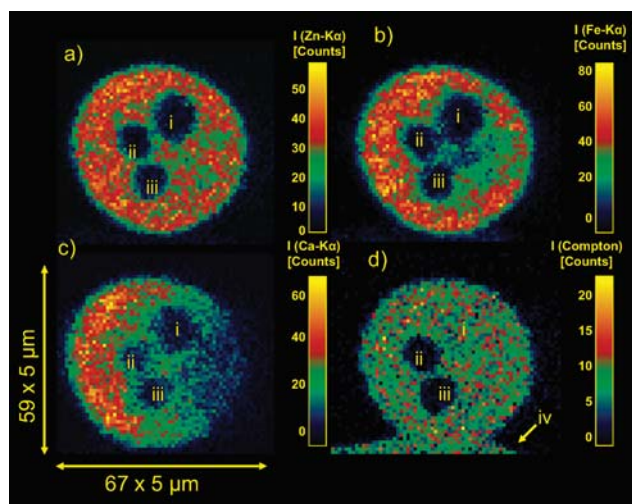
cavities and for this lower Z element a clear presence of self-absorption effects can be observed from the left side towards the right side of the sample (Fig. 9.c).

A striking result is emerging from the analysis of the Compton scattering signal. The cavities shown in Fig. 9.d.ii and Fig. 9.d.iii show very low intensity Compton scattering, which is a good indication for the above mentioned assumption that these are hollow cavities. The cavity shown in Fig. 9.d.i, however, shows a similar scattering intensity as the rest of the sample matrix. This indicates that a material is present in this cavity with a similar density as the rest of the sample, but in which no Zn, Fe and Ca can be detected anymore. Our assumption is that during the sample preparation the HMDS drying agent filled some of the cavities within the sample, resulting in a similar Compton scattering intensity, but containing a very low concentration of detectable higher-Z elements. This also shows that during the sample preparation little or no leaching of the metals into the drying agent occurs. Another interesting effect can be observed when comparing the size of *e.g.* the cavity shown in Fig. 9.a–d.iii. It can be observed that the diameter seems to increase with respect to higher energy fluorescent lines (Ca-K$_\alpha$, Fe-K$_\alpha$, Zn-K$_\alpha$), which is in perfect agreement with the smaller acceptance (or higher resolution) of the detection side capillary at higher energies.

For the 3D confocal μ-XRF analyses, a total of 16 sections were scanned across the centre of the egg. This 3D scan resulted in a total of 63248 single XRF spectra, obtained within a total analysis time of approximately 20 h, even with a measuring time of 1s per point only and using a dynamic scanning mode. Fig. 10 shows 16 adjacent planes measured through the sample, each 10 μm apart, visualising the Zn elemental distribution in depth. From the image, one can observe hollow areas changing in position and in size, revealing the gain in information which is obtained when extending the scanning algorithm to a third dimension. In order to get a 3D interpretation, the dataset was read in with the IDL software package[30] and an appropriate opacity setting and thresholding was applied in order to visualise a given isosurface within the egg, as illustrated for the Fe distribution (see Fig. 11, θ = 0°). For full information, the more

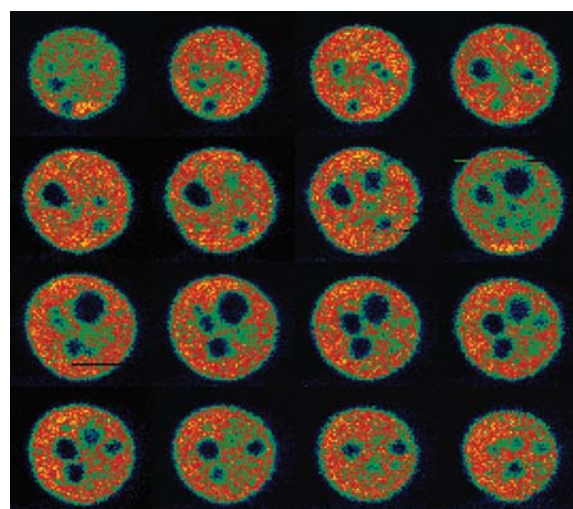**Fig. 9** Overview of the Zn (a), Fe (b), Ca (c) elemental distributions and Compton scattering signal (d) through a single egg of *Daphnia magna*. i, ii and iii represent hollow areas whereas iv refers to the position of the glue between the egg and the carbon fibre.

Fig. 10 Overview of the Zn elemental distributions in the 16 planes through an egg of *Daphnia magna*.

This journal is © The Royal Society of Chemistry 2010

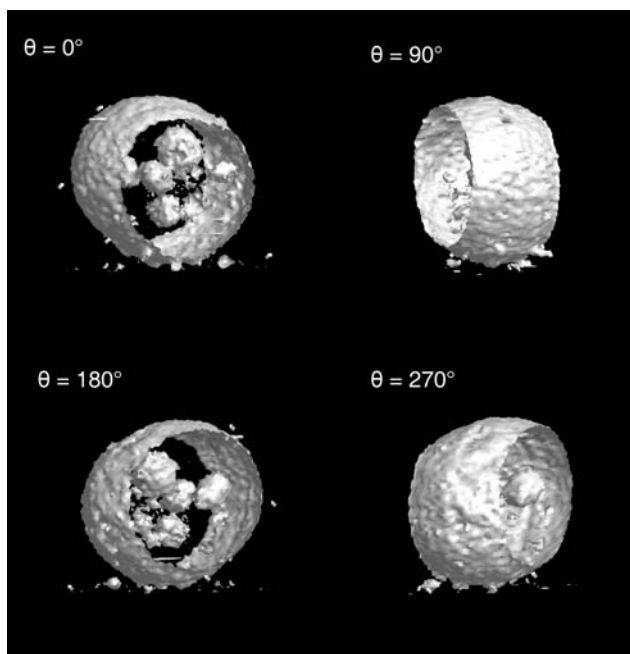*J. Anal. At. Spectrom.*, 2010, **25**, 544–553 | 551

Fig. 11 Rendered Fe isosurface under 4 different angles.

dense part of the egg are made transparent, in order to visualise the internal structure of the sample. One can now clearly see that the central portion of the spherical sample was analysed. Through the 3D visualisation the internal cavities can clearly be observed, including the iron grains under the sample mixed with the glue. Also, it can now be observed that 5 cavities are present inside the sample, which is hard to conclude from the 2D data. For further inspection, the sample can also be rotated to an angle of interest, as illustrated in Fig. 11 (θ = 90, 180, 270°).

However, in order to compare the spatial 3D distribution of elements, different isosurfaces have to be compared, which can be a cumbersome task. Therefore, the isosurfaces of the analytical signals of interest (*e.g.* Zn, Fe and Compton scattering) were each assigned an individual color channel (red, green and blue) as illustrated in Fig. 12.a–c. The RGB representation shown in Fig. 12.d then delivers a full 3D multi elemental trace level representation of the sample investigated. For full information, a color triangle was added to the image. One can clearly observe
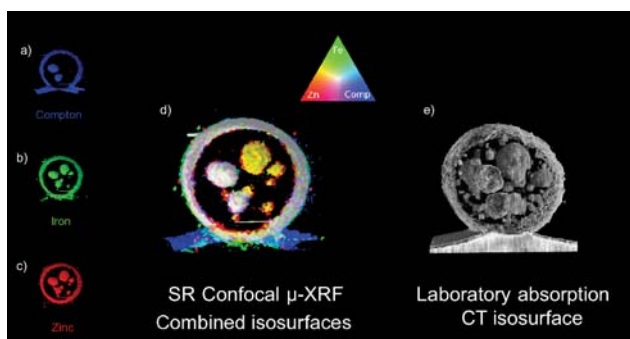

Fig. 12 a) Compton scattering isosurface. b) Iron isosurface. c) Zinc isosurface. d) RGB isosurface combining the Compton scattering, Fe and the Zn isosurface. e) Absorption micro-CT scan of the corresponding sample.

a white isosurface around the sample, indicating a transition from the scattering sample containing trace level metals towards the air. A similar transition can be observed for the 3 cavities on the left side of Fig. 12.d. Also two other cavities are appearing in yellow on the right side of Fig. 12.d, which means that an interface is present where there is a sudden drop in trace level presence of Zn and Fe, but that the Compton scattering is continuous. This is perfectly matching the above mentioned polymer diffusion in some of the cavities of the sample, which was also observed in the absorption micro-CT measurements. From the image, the Compton scattering isosurface at the bottom clearly corresponds to the surface of the glue, whereas Fe hotspots can be observed inside it. For full 3D element-to-tissue correlation, a micro absorption CT rendering of the very same sample is visualised in Fig. 12.e, which is in good agreement with the confocal data. Indeed, also here different cavities are observed with even a slight difference in density. From comparison with the 3D confocal μ-XRF data, it is possible to assign elemental contents to each 3D structure.

Conclusions and outlook

In this manuscript, synchrotron radiation based scanning X-ray fluorescence and laboratory based X-ray absorption techniques were applied in an ecotoxicological case study. Emphasis was placed on the powerful role that synchrotron radiation confocal micro X-ray fluorescence can play in the 3D non-destructive elemental analysis of delicate biological samples. Due to the relatively simple sample alignment, more efficient and thus lower measuring time, a general overview of the trace level metal distributions of a virtual section through a biological specimen can be obtained within a fairly short acquisition time. The aforementioned aspects, combined with a 2D dynamic scanning mode, allow analysing and comparing the elemental concentrations of several samples from a full factorial design in a single experimental session. Afterwards, certain regions of interest can be studied in greater detail using smaller step sizes to improve the resolution of the image (*e.g.* down to 5 μm) and/or longer measuring times to obtain quantitative data. We also illustrate that with the confocal technique, the element distributions in different perpendicular planes of interest can be visualised. These 2D element distributions can be combined with a full 3D absorption density model, revealing the presence of metals in the different tissues. Moreover, by applying an accelerated dynamic scanning mode, full 3D trace level elemental distributions within delicate biological specimens can be obtained. A full 3D element-to-tissue correlation on the micrometer level is then obtained when this 3D element confocal data are coupled with laboratory micro absorption computed tomography.

Acknowledgements

552 | *J. Anal. At. Spectrom.*, 2010, **25**, 544–553

This journal is © The Royal Society of Chemistry 2010

References

1 G. Silversmit, B. Vekemans, F. E. Brenker, S. Schmitz, M. Burghammer, C. Riekel and L. Vincze, *Anal. Chem.*, 2009, **81**(15), 6107–6112.

2 C. G. Schröer, O. Kurapova, J. Patommel, J. Feldkamp, B. Lengeler, M. Burghammer, C. Riekel, L. Vincze, A. Van der Hart and M. Küchler, *Appl. Phys. Lett.*, 2005, **87**, 124103.

3 B. De Samber, G. Silversmit, R. Evens, K. De Schamphelaere, C. Janssen, B. Masschaele, L. Van Hoorebeke, L. Balcaen, F. Vanhaecke, G. Falkenberg and L. Vincze, *Anal. Bioanal. Chem.*, 2008, **390**, 267–271.

4 B. De Samber, R. Evens, K. De Schamphelaere, G. Silversmit, B. Masschaele, T. Schoonjans, B. Vekemans, C. Janssen, L. Van Hoorebeke, I. Szaloki, F. Vanhaecke, G. Falkenberg and L. Vincze, *J. Anal. At. Spectrom.*, 2008, **23**, 829–839.

5 K. De Schamphelaere, M. Canli, V. Van Lierde, I. Forrez, F. Vanhaecke and C. Janssen, *Aquat. Toxicol.*, 2004, **70**, 233–244.

6 K. De Schamphelaere and C. Janssen, *Environ. Toxicol. Chem.*, 2004, **23**, 2038–2049.

7 L. Balcaen, K. De Schamphelaere, C. Janssen, L. Moens and F. Vanhaecke, *Anal. Bioanal. Chem.*, 2008, **390**, 555–569.

8 P. Paquin, J. Gorsuch, S. Apte, G. Batley, K. Bowles, P. Campbell, C. Delos, D. Di Toro, R. Dwyer, F. Galvez, R. Gensemer, G. Goss, C. Hogstrand, C. Janssen, J. MCGeert, R. Naddy, R. Playle, R. Santore, U. Schneider, W. Stubblefield, C. Wood and K. Wu, *Comp. Biochem. Physiol., Part C: Toxicol. Pharmacol.*, 2002, **133**, 3–35.

9 D. Heijerick, K. De Schamphelaere and C. Janssen, *Environ. Toxicol. Chem.*, 2002, **21**, 1309–1315.

10 L. Vincze, B. Vekemans, F. Brenker, G. Falkenberg, K. Rickers, A. Somogyi, M. Kersten and F. Adams, *Anal. Chem.*, 2004, **76**, 6786–6791.

11 B. Muyssen, K. De Schamphelaere and C. Jansen, *Aquat. Toxicol.*, 2006, **77**, 393–401.

12 C. Laforsch and R. Tollrian, *Archiv für Hydrobiologie*, 2000, **149**, 587–596.

13 G. Falkenberg, Characterization of a Strongly Focussing Capillary Half-lens, *Hasylab Annual Report*, 2006, **1**.

14 B. De Samber, G. Falkenberg and L. Vincze, *Hasylab Annual Report*, 2005, **1**, 1389–1390.

15 Octopus, Scanner independent CT reconstruction software for fan beam, cone beam and parallel beam geometry, www.xraylab.com.

16 B. Kanngieser and W. Malzer, *Spectrochim. Acta, Part B*, 2005, **60**, 1334–1341.

17 G. Falkenberg, R. Dietsch, U. Fittschen, R. Simon and D. Weissbach, *Hasylab Annual Report*, 2007, **1**, 1619–1620.

18 B. Vekemans, K. Janssens, L. Vincze, F. Adams and P. Van Espen, *Spectrochim. Acta, Part B*, 1995, **50**, 149–169.

19 A. Brunetti, M. Sanchez del Rio, B. Golosio, A. Simionovici and A. Somogyi, *Spectrochim. Acta, Part B*, 2004, **59**, 1725–1731.

20 R. Pirow, F. Wollinger and R. Paul, *The Journal of Experimental Biology*, 1999, **202**, 3089–3099.

21 R. Pirow, F. Wollinger and R. Paul, *The Journal of Experimental Biology*, 1999, **202**, 553–562.

22 M. Barron and S. Albeke, *Aquat. Toxicol.*, 2000, **50**, 257, 264.

23 C. Hogstrand, S. Reid and C. Wood, *Journal of Experimental Biology*, 1995, **198**, 337–348.

24 C. Hogstrand, P. Verbost, S. Wendelaar Bonga and C. Wood, *American Journal of Physiology*, 1996, **270**, 1141–1147.

25 M. Seidl, R. Pirow and J. Rüdiger, *Zoology*, 2002, **105**, 15–23.

26 B. Golosio, A. Somogyi, A. Simionovici, P. Bleuet and J. Susini, *Appl. Phys. Lett.*, 2004, **84**, 1–3.

27 B. Golosio, A. Simionovici and A. Somogyi, *J. Appl. Phys.*, 2003, **94**, 145–150.

28 B. Vekemans, L. Vincze, F. E. Brenker and F. Adams, *J. Anal. At. Spectrom.*, 2004, **19**, 1302–1308.

29 VGStudio MAX, www.volumegraphics.com.

30 Interactive Data Language, www.ittvis.com.

31 T. Trojek and T. Cechak, K-alpha/K-beta ratios of fluorescence X-rays as an information source on the depth Distribution of iron in a low Z matrix, *Anal. Sci.*, 2008, **24**, 851–854.

This journal is © The Royal Society of Chemistry 2010

J. Anal. At. Spectrom., 2010, **25**, 544–553 | 553